Journal of the Ceramic Society of Japan 134 [4] 303-310 2026
DOI https://doi.org/10.2109/jcersj2.25153

JCS-Japan

FULL PAPER

First-principles study on electronic structure and optical properties of Mn-doped $Ba_3V_2O_8$

Hiroki Kojima[1,2], Taiyo Inada[1,2], Shigenori Matsushima[3,4,†], Junko Ishii[3], Kenji Obata[3] and Masao Arai[5]

[1] Advanced Course of Creative Engineering, National Institute of Technology, Kitakyushu College, 5–20–1 Shii, Kokuraminami-ku, Kitakyushu, 802–0985, Japan
[2] Department of Interdisciplinary Engineering, Faculty of Engineering, Kyushu University, 6–1 Kasugakoen, Kasuga, Fukuoka 816–8580, Japan
[3] Department of Creative Engineering, National Institute of Technology, Kitakyushu College, 5–20–1 Shii, Kokuraminami-ku, Kitakyushu, 802–0985, Japan
[4] Department of Collaborative Interdisciplinary Engineering Sciences, Faculty of Engineering Science, Kyushu University, 6–1 Kasugakoen, Kasuga, Fukuoka 816–8580, Japan
[5] Center for Basic Research on Materials, National Institute for Materials Science (NIMS), 1–1 Namiki, Tsukuba, Ibaraki 305–0044, Japan

The electronic structure and optical properties of Mn-doped $Ba_3V_2O_8$, a promising cobalt-free pigment, are investigated using first-principles calculations to elucidate the microscopic mechanism of its vivid blue coloration. Structural optimization done by the pseudopotential method, combined with high-precision all-electron band calculations (FLAPW method) reveals the interplay between local lattice distortion and optical response. The results demonstrate that the substitution of V^{5+} with Mn^{5+} ($3d^2$) introduces spin-polarized impurity states within the band gap. These mid-gap states arise intrinsically from the crystal field splitting of the Mn orbitals into occupied e and unoccupied t_2 levels. Crucially, the $[MnO_4]^{3-}$ tetrahedra undergo significant structural distortion, lowering the local symmetry from T_d to C_1. While this distortion is not the primary origin of the impurity levels, it plays a decisive role in governing the optical transition probabilities. The symmetry breaking enhances the hybridization between Mn 3d and O 2p orbitals, relaxing the selection rules for d–d transitions. Consequently, a distinct absorption peak arises at approximately 1.6 eV, which is responsible for the blue color, alongside a charge-transfer transition around 3.3 eV. Furthermore, the distortion induces strong optical anisotropy, manifested as a significant splitting of the dielectric function along the principal optical axes. This study provides a comprehensive theoretical framework linking the local geometric distortion to the intense and anisotropic optical response of Mn-doped $Ba_3V_2O_8$.

Key-words : $Ba_3V_2O_8$, Mn-doped $Ba_3V_2O_8$, First-principles calculation

[Received November 10, 2025; Accepted January 27, 2026; Published online March 5, 2026]

1. Introduction

Ceramic pigments have historically relied on hazardous metallic elements such as hexavalent chromium (Cr), cadmium (Cd), antimony (Sb), and lead (Pb) to achieve vibrant colors. In recent years, however, growing concerns about the detrimental effects of these metals on human health and the environment have prompted calls for stringent international regulations on their use, as exemplified by Europe's RoHS Directive.[1)] The most widely utilized blue ceramic pigment, cobalt blue ($CoAl_2O_4$), serves as a case in point. While $CoAl_2O_4$ offers excellent blue coloration, easy synthesis, and superior resistance to heat, acid, and alkali, cobalt (Co) is not only a rare and expensive element but also poses significant toxicity risks. For these compelling reasons—spanning public health, environmental preservation, and economic viability—the development of cobalt-free blue ceramic pigments has become an urgent scientific and industrial challenge.

Recently, Smith et al. reported that $YIn_{1-x}Mn_xO_3$ exhibits a vivid blue color, presenting it as a potential substitute for $CoAl_2O_4$.[2)] Unfortunately, indium (In), which is in high demand for transparent conductive films, is even rarer and more expensive than Co, rendering its wide spread application as a pigment economically impractical. An alternative and promising route involves oxides and phosphates doped with pentavalent manganese (Mn^{5+}), which have been repeatedly shown to exhibit blue coloration.[3–6)] Among these materials, Mn-doped $Ba_3V_2O_8$, discovered by Guo et al.,[7)] is particularly noteworthy as a potential $CoAl_2O_4$ replacement due to its superior thermal stability and durability.

A key factor contributing to the promise of this material

† Corresponding author: S. Matsushima; E-mail: smatsu@kct.ac.jp

is the high degree of similarity between the V^{5+} and Mn^{5+} ions that occupy the tetrahedral sites in the $Ba_3V_2O_8$ host lattice. These ions share the same valence state and have only a small difference in ionic radius. Furthermore, both readily adopt a tetrahedral coordination with four surrounding oxygen atoms. This crystallographic compatibility facilitates a wide range of manganese solid solution concentrations, which in turn enables continuous tuning of the material's color tone.

Despite its potential, a fundamental understanding of the solid-state electronic structures of both the undoped $Ba_3V_2O_8$ unit cell and the Mn-doped $Ba_3V_2O_8$ supercell, which are intrinsically linked to the coloration mechanism, remains elusive. Therefore, this study aims to comprehensively elucidate these electronic structures by performing first-principles band calculations, thereby providing a theoretical foundation for the material's observed optical properties in details. Some preliminary data and interpretations were previously published elsewhere.[8] In this paper, we present revised figures and extended datasets, along with newly obtained insights that were not included in the previous report.

2. Computational methods

The initial crystallographic information for undoped $Ba_3V_2O_8$ was sourced from literature values registered in the ICSD database.[9] The $Ba_3V_2O_8$ unit cell belongs to the space group *R*3-*m* (No. 166) and features five distinct Wyckoff positions occupied by Ba1, Ba2, V, O1, and O2, as depicted in **Fig. 1**(a). Furthermore, Fig. 1(b) presents the first Brillouin zone of $Ba_3V_2O_8$ primitive unit cell.

Our computational approach involved a two-step process. First, structural optimizations were performed using the CASTEP (Cambridge Sequential Total Energy Package) program,[10] a first-principles molecular dynamics package well-suited for efficient geometry relaxation. During the optimization of undoped $Ba_3V_2O_8$, the *R*3-*m* space group symmetry was maintained. The exchange–correlation interaction was treated within the generalized gradient approximation (GGA) using the PBE functional.[11,12] Convergence criteria for the optimization were stringently set as follows: a total energy change of 1.0×10^{-5} eV/atom, a maximum atomic force of 3.0×10^{-2} eV/Å, a maximum displacement of 1.0×10^{-3} Å, and a maximum stress of 5.0×10^{-2} GPa. A plane-wave basis set with a cutoff energy of 340 eV was employed, and the valence electrons were described using Vanderbilt-type non-local ultra-soft pseudopotentials.[13] Integration in the reciprocal space of the first Brillouin zone was performed using a $5 \times 5 \times 2$ Monkhorst-Pack mesh,[14] yielding 7 irreducible *k*-points. For the Mn-doped system, a $2 \times 2 \times 1$ supercell was constructed from the optimized undoped unit cell, and one V atom was subsequently substituted with an Mn atom. Due to the symmetry breaking induced by the dopant, the space group of the system was treated as *P*1. In this case, only the atomic coordinates of the supercell were optimized, while the lattice parameters were fixed to those of the undoped host to simulate a dilute doping condition. The same GGA functional, convergence criteria, and cutoff energy were used, while *k*-point sampling was restricted to the Γ-point, a common practice for large supercell calculations.

Following structural optimization, electronic-structure and optical-property calculations were carried out using WIEN2k,[15,16] which implements the full-potential linearized augmented plane wave plus local orbital (FLAPW+*lo*) method. This choice was motivated by the need for highly accurate all-electron wavefunctions to analyze optical absorption in direct relation to the complex dielectric function and density of states (DOS). Unlike pseudopotential methods, WIEN2k provides precise projected DOS (PDOS) and momentum matrix elements between occupied and unoccupied states, which are essential for interpreting absorption features above the valence band. The hexagonal lattice parameters optimized by CASTEP were adopted, and atomic coordinates were converted to the rhombohedral representation for WIEN2k input. The basis set consisted of linear combinations of spherical harmonics within the Muffin-Tin (MT) regions and plane waves in the interstitial region. For undoped $Ba_3V_2O_8$, the MT sphere radii were set to 2.50, 1.68, and 1.52 a.u. for Ba, V, and O, respectively. The plane wave

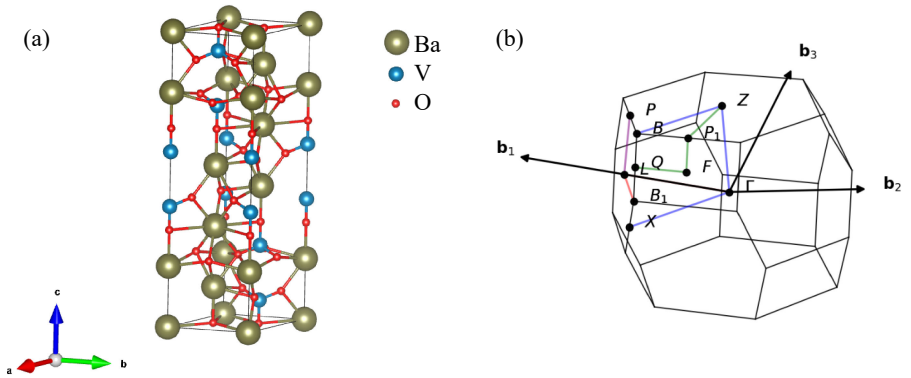

Fig. 1. Crystal structure of $Ba_3V_2O_8$ (*R*3-*m*) and the Brillouin zone of its primitive unit cell. High-symmetry points are shown as fractional coordinates: Γ(0, 0, 0), L(0.5000, 0, 0), B_1(0.5000, 0.2038, −0.2038), B(0.7962, 0.5000, 0.2038), Z(0.5000, 0.5000, 0.5000), X(0.3519, 0, −0.3519), Q(0.6481, 0.3519, 0), F(0.5000, 0.5000, 0), P_1(0.6481, 0.6481, 0.2038), P(0.7962, 0.3519, 0.3519).

Table 1. Lattice constants and atomic coordinates of $Ba_3V_2O_8$ unit cell before and after structural optimization

	a [Å]	c [Å]	atom site label	atom site fract x	atom site fract y	atom site fract z
Before structural optimization	5.7843	21.3274	Ba1	0.0000	0.0000	0.0000
			Ba2	0.0000	0.0000	0.2051
			V1	0.0000	0.0000	0.4063
			O1	0.0000	0.0000	0.3279
			O2	0.1614	−0.1614	0.5655
After structural optimization	5.8676	21.5183	Ba1	0.0000	0.0000	0.0000
			Ba2	0.0000	0.0000	0.2056
			V1	0.0000	0.0000	0.4072
			O1	0.0000	0.0000	0.3279
			O2	0.1604	−0.1604	0.5659

cutoff was defined by $R_{MT} \times K_{max} = 7.0$, and 44 k-points were used for sampling. For the Mn-doped supercell, the MT radii were 5.45, 1.76, 1.68, and 1.51 a.u. for Ba, Mn, V, and O, respectively, with a plane wave cutoff of $R_{MT} \times K_{max} = 5.0$ and 54 k-points. The exchange–correlation interaction was consistently treated using the GGA functional.

The optical properties were derived from the complex dielectric function tensor, $\varepsilon(\omega) = \varepsilon_1(\omega) + i\varepsilon_2(\omega)$.[17] The imaginary part, $\varepsilon_2(\omega)$, was computed using the sum-over-states approach based on momentum matrix elements between occupied and unoccupied states, while $\varepsilon_1(\omega)$ was obtained via the Kramers–Kronig relation. To ensure the convergence of the optical spectra and eliminate numerical artifacts arising from k-point discretization, a dense k-mesh (resulting in 128 k-points) was employed for the optical properties calculation of Mn-doped $Ba_3V_2O_8$ supercell. In addition, the upper energy limit (E_{max}) for the band calculation was set to 5.0 Ry (68.03 eV). Consequently, a maximum of 1102 energy bands for the undoped $Ba_3V_2O_8$ were included in the calculation, which comprises 571 occupied bands. In contrast, the Mn-doped $Ba_3V_2O_8$ system required considering 4599 bands at most, and the number of occupied bands was 4182. The absorption coefficient $I(\omega)$ was estimated using the following equation;

$$I(\omega) = (\sqrt{2}\omega/c)\left[\sqrt{\varepsilon_1(\omega)^2 + \varepsilon_2(\omega)^2} - \varepsilon_1(\omega)\right]^{1/2} \quad (1)$$

where c is the speed of light in a vacuum.[18] The calculated spectra were broadened using Lorentzian functions to facilitate comparison with experimental observations.

3. Results and discussion

Table 1 presents the lattice parameters and atomic coordinates for undoped $Ba_3V_2O_8$ before and after structural optimization, with all values reported in a hexagonal representation. The optimization led to minor changes in the lattice parameters: the a-axis increased by approximately 1.4 %, and the c-axis increased by roughly 0.9 %. This slight overestimation of lattice constants is a well-known characteristic of the GGA functional and indicates that our structural model is physically sound.[19] A detailed comparison of the local coordination environments is provided

Table 2. Bond distances (Ba1–O, Ba2–O, V–O, Mn–O) of $Ba_3V_2O_8$ unit cell and Mn-doped $Ba_3V_2O_8$ supercell after structural optimization

	$Ba_3V_2O_8$			Mn-doped $Ba_3V_2O_8$
	Ba1–O	Ba2–O	V–O	Mn–O
Bond length (Å)	2.7913 × 6	2.6297	1.7079	1.7437
		2.8607 × 3	1.7292 × 3	1.7700
		2.9911 × 6		1.7701
				1.7708

Table 3. Comparison of bond angles in $[VO_4]^{3-}$ and $[MnO_4]^{3-}$ tetrahedra

	$[VO_4]$	$[MnO_4]$
Bond angle (°)	109.41	108.03
	109.41	109.22
	109.41	109.22
	109.53	109.23
	109.53	109.23
	109.53	111.83

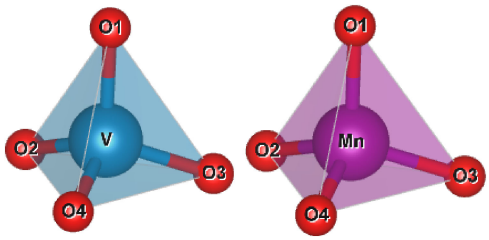

in **Table 2**, which lists the metal-oxygen bond distances for the optimized structures of both undoped $Ba_3V_2O_8$ and the Mn-doped supercell. In the undoped host, each V atom is tetrahedrally coordinated by four oxygen atoms, with two distinct V–O distances. Upon substitution of V with Mn, all Mn–O bond distances are found to be longer than their V–O counterparts. Furthermore, the difference between the longest and shortest Mn–O distances is greater than that for the V–O bonds, suggesting an increase in geometric distortion. This observation is corroborated by the bond angle analysis in **Table 3**, which compares six distinct O–V (or Mn)–O angles within the $[VO_4]^{3-}$ and $[MnO_4]^{3-}$ tetrahedra. The angular distribution confirms that the $[VO_4]^{3-}$ tetrahedron more closely approaches an

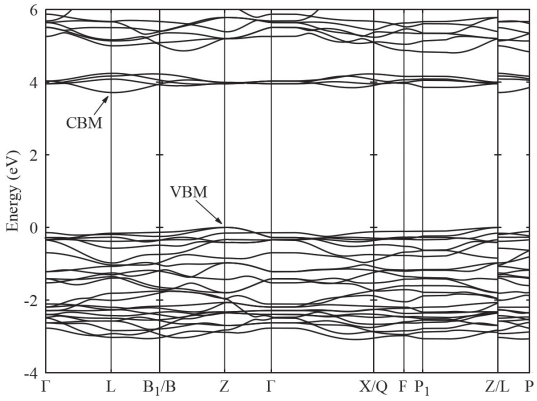

Fig. 2. Calculated energy band structure of $Ba_3V_2O_8$ primitive unit cell.

ideal regular tetrahedron than the $[MnO_4]^{3-}$ unit does. Collectively, the results in Tables 2 and 3 provide clear evidence that the $[MnO_4]^{3-}$ tetrahedron is structurally more distorted than the original $[VO_4]^{3-}$ tetrahedron it replaces.

Figure 2 displays the calculated electronic band structure of undoped $Ba_3V_2O_8$. For the energy band calculation, highly symmetric *k*-points within the first Brillouin zone were investigated as indicated in the literature,[20] and four directions—Γ–L–B1, B–Z–Γ–X, Q–F–P1–Z, and L–P—were selected. The calculation reveals that the valence band maximum (VBM) is located at the Z point, while the conduction band minimum (CBM) resides at the L point, classifying undoped $Ba_3V_2O_8$ as an indirect band gap semiconductor. Although standard GGA functionals typically underestimate electronic band gaps,[21,22] the computed value of 3.6 eV shows excellent agreement with the experimental optical gap of 3.59 eV.[7] Such agreement in vanadate systems has been observed elsewhere and is often attributed to a fortuitous error cancellation unique to the V 3d–O 2p charge-transfer nature, or to the fact that the experimental optical gap includes significant excitonic binding energies not captured in the single-particle GGA gap.[23,24] Regardless of the absolute value, our focus remains on the relative changes in electronic structure induced by Mn doping, which are reliably described at this level of theory. To ensure a meaningful comparison between the electronic structures of undoped and Mn-doped $Ba_3V_2O_8$, the energy axes were aligned using the Ba 5p core-level states as a common reference. **Figure 3** shows the DOS of undoped $Ba_3V_2O_8$. The site-projected DOS presented here corresponds to the total density of states integrated within the muffin-tin sphere of each atomic species, which encompasses the contributions from all angular momentum components. To ensure a clear physical interpretation, all DOS data are consistently normalized per atom. Analysis of the DOS confirms that the valence band is predominantly composed of O 2p states, while the lower part of the conduction band is mainly derived from V 3d states. The splitting observed in the V 3d states is a direct consequence of the crystal field imposed by the $[VO_4]^{3-}$ tetrahedral environment. The introduction of Mn dramatically alters this electronic landscape, as shown in **Fig. 4**, which illustrates the total DOS (TDOS) and Mn-related PDOS for the Mn-doped supercell. The most striking feature is the appearance of new impurity levels within the fundamental band gap of $Ba_3V_2O_8$, originating from the Mn 3d states. A comparison between the spin-up and spin-down channels reveals that the up-spin peak lies at a lower energy, indicating that this is the majority spin states and that the system is spin-polarized. Specifically, the majority-spin Mn 3d states form impurity levels within the host gap which are split into distinct occupied and unoccupied bands. The lower-energy component of the spin-up states is completely occupied by electrons, and the Fermi level ($E = 0$) is pinned precisely at the maximum of this occupied level. The energy difference between these mid-gap states and the VBM is smaller than the photon energies of visible light. This electronic configuration suggests that the incorporation of Mn enables not only intra-atomic d–d transitions between the occupied and unoccupied Mn 3d states but also charge-transfer (CT) type absorption from the O 2p-dominated valence band to these Mn 3d states.

These modifications to the electronic structure manifest directly in the optical properties. **Figure 5** presents the calculated real and imaginary parts of the complex dielectric function, $\varepsilon_1(\omega)$ and $\varepsilon_2(\omega)$, for both undoped and Mn-doped $Ba_3V_2O_8$. As a hexagonal crystal, undoped $Ba_3V_2O_8$ is optically uniaxial, characterized by two independent dielectric tensor components (*xx* and *zz*). In contrast, the Mn-doped supercell, with its lower P_1 space group symmetry, becomes optically biaxial, possessing six tensor components (three diagonal and three off-diagonal). While the static refractive indices $[\varepsilon_1(0)]$ are similar for both systems, the absorptive part, $\varepsilon_2(\omega)$, reveals critical differences. The overall shape of the $\varepsilon_2(\omega)$ curve for the doped system resembles the undoped one, but with the crucial addition of two new features: a small, broad peak around 1.6 eV and a more pronounced peak near 3.3 eV, both directly attributable to the presence of Mn. Based on the DOS analysis, the absorption at 1.6 eV is assigned to the spin-allowed d–d transitions within the Mn 3d manifold, while the peak at 3.3 eV corresponds to the charge-transfer (CT) transitions from O 2p to Mn 3d states.

These features are more clearly resolved in the optical absorption spectra $I(\omega)$, shown in **Fig. 6**. Undoped $Ba_3V_2O_8$ exhibits a sharp absorption onset around 3.6 eV, corresponding to interband transitions from the valence to the conduction band. Conversely, the Mn-doped system displays distinct absorption peaks at the same energies identified in the $\varepsilon_2(\omega)$ spectrum. Since the Mn-doped system possesses low symmetry (P_1), the dielectric function is a tensor with non-zero off-diagonal components in the crystallographic coordinate system. However, considering that ceramic pigments are practically utilized in powder form consisting of randomly oriented crystallites, the macroscopic optical properties are best described by considering the optical response along the principal axes and their polycrystalline average. Therefore, we diagonalized the calculated frequency-dependent complex dielectric ten-

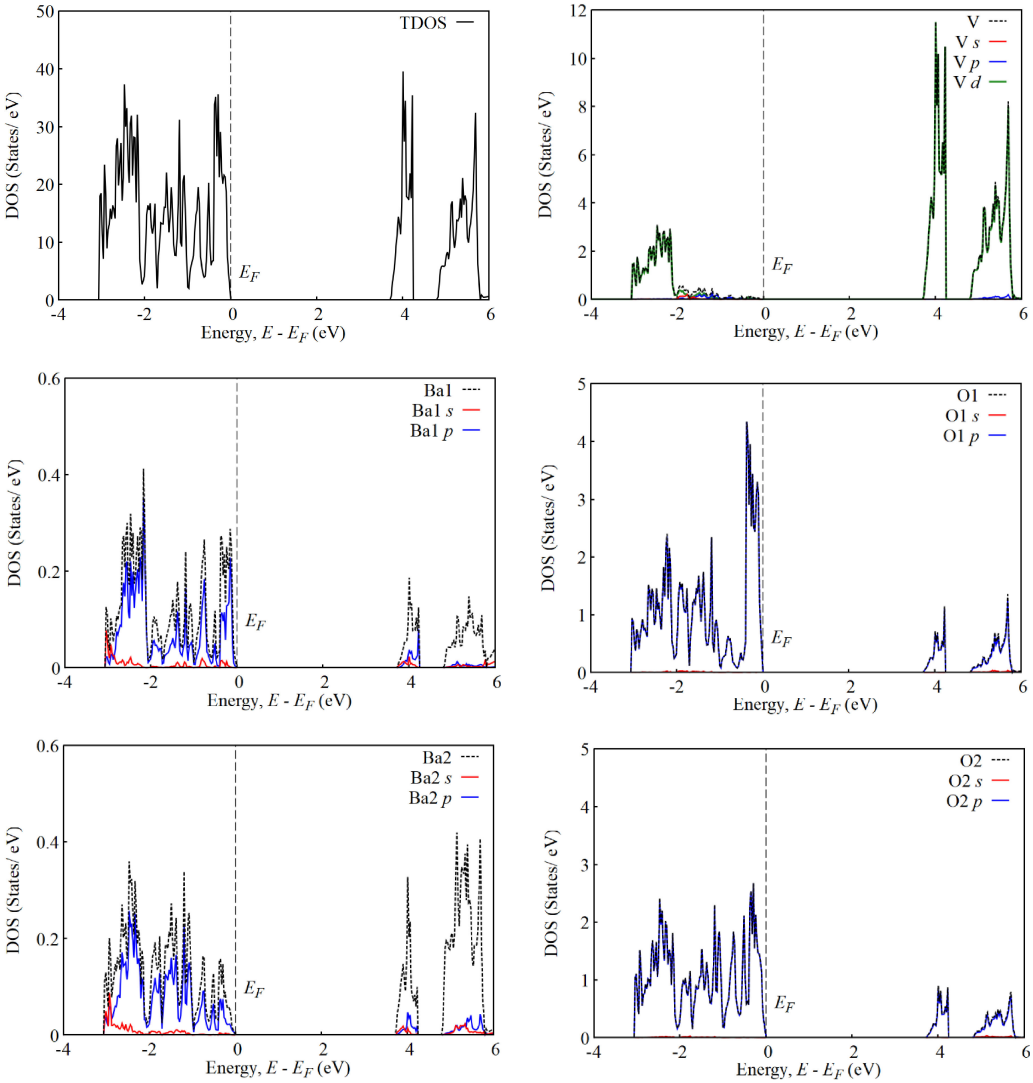

Fig. 3. Total density of states (TDOS) and site-projected DOS for pristine $Ba_3V_2O_8$: TDOS, Ba1, Ba2, V, O1, and O2. The dashed line marks the Fermi level (E_F).

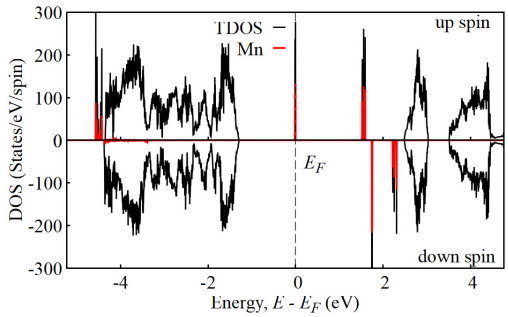

Fig. 4. Total density of states (TDOS) and Mn 3*d* projected density of states (PDOS) for the Mn-doped $Ba_3V_2O_8$ supercell. The dashed line indicates the Fermi level (E_F).

sor at each energy point to obtain the eigenvalues along the three principal optical axes. Based on these principal dielectric functions, we determined the absorption coefficients $\alpha_1(\omega)$, $\alpha_2(\omega)$, and $\alpha_3(\omega)$, and corresponding to each principal axis, as well as the orientation-averaged absorption spectrum.

Figure 6 also includes the absorption spectrum calculated for the Mn-doped structure prior to structural optimization to investigate the influence of local distortion. The "unoptimized" structure is defined as the host $Ba_3V_2O_8$ supercell ($2 \times 2 \times 1$) where one V atom is simply substituted by Mn without relaxing the atomic coordinates, thus preserving the quasi-ideal tetrahedral environment. Comparing the optimized and unoptimized spectra reveals a striking difference. In the unoptimized structure, the absorption intensity in the visible region is low, and the anisotropy is weak. However, when the structural distortion is introduced through optimization, the absorption peak originating from the transition around 1.6 eV is drastically enhanced. Furthermore, the splitting among the three principal components $\alpha_1(\omega)$, $\alpha_2(\omega)$, and $\alpha_3(\omega)$ expands significantly. The spectrum originating from the CT absorption around 3.3 eV also becomes distinct. This behavior indicates that the optical anisotropy and the intensity of the transitions are intrinsically linked. The large splitting of the principal components in the optimized

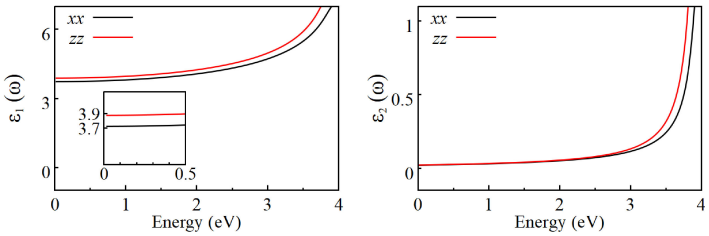

(a) $Ba_3V_2O_8$ unit cell

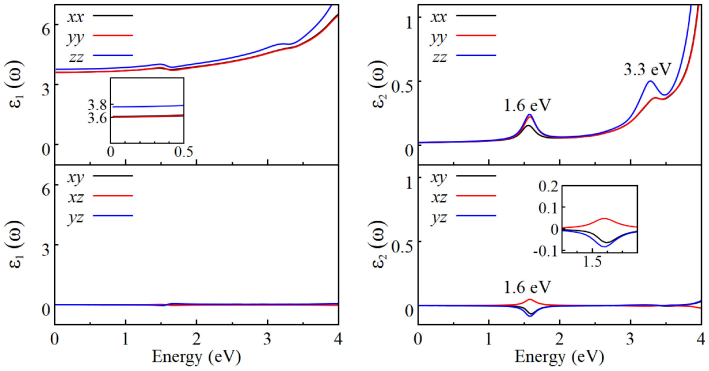

(b) Mn-doped $Ba_3V_2O_8$ supercell

Fig. 5. Complex dielectric function of $Ba_3V_2O_8$ unit cell and Mn-doped $Ba_3V_2O_8$ supercell.

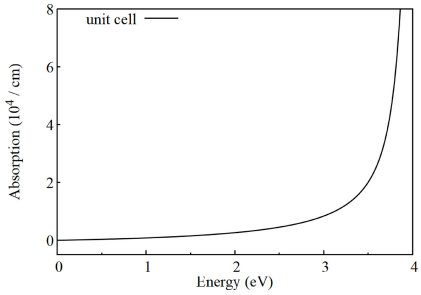

(a) Undoped

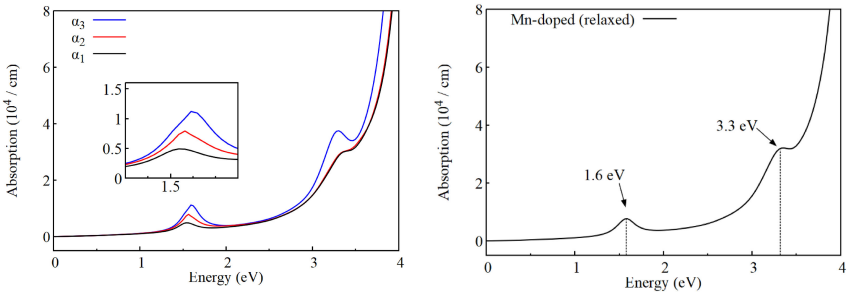

(b) Mn-doped (optimized)

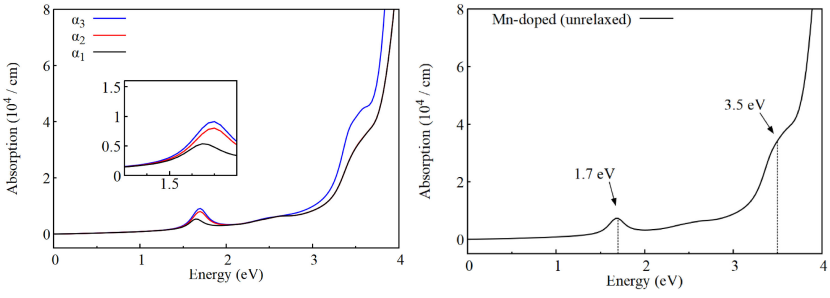

(c) Mn-doped (unoptimized)

Fig. 6. Optical absorption coefficients of $Ba_3V_2O_8$ unit cell and Mn-doped $Ba_3V_2O_8$ supercell.

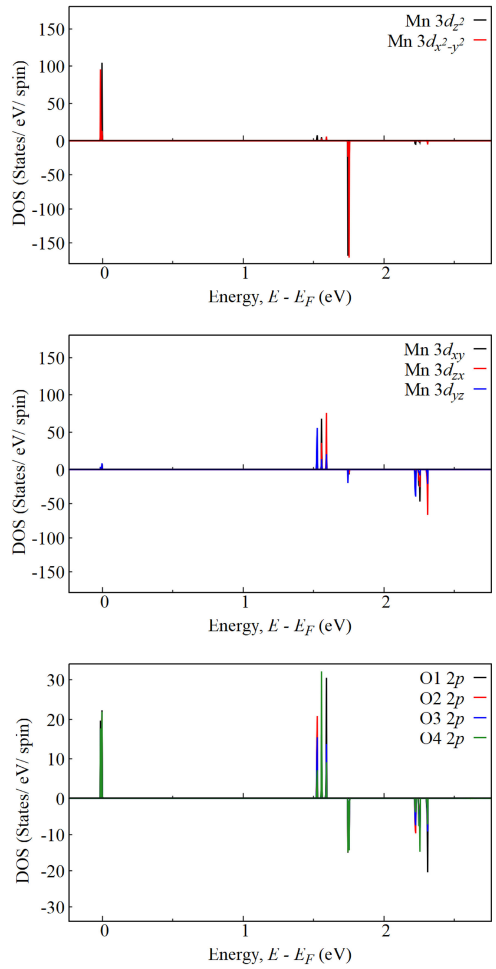

Fig. 7. Projected density of states for individual Mn 3d orbitals and the total O 2p states integrated over oxygen sites O1 through O4 in the Mn-doped $Ba_3V_2O_8$ supercell.

structure is the physical manifestation of the significant off-diagonal terms present in the original lattice coordinate system. These results indicate that the introduction of Mn onto the V site not only forms split 3d levels within the band gap but also that the vivid blue color is effectively "switched on" by the local distortion of the $[MnO_4]^{3-}$ unit.

To provide a microscopic understanding of the absorption features observed in the principal absorption coefficients, we analyzed the PDOS of the Mn atom in the local coordinate system (**Fig. 7**). In a perfect T_d field, the Mn 3d orbitals split into a lower-energy doubly degenerate e set (d_z^2, $d_{x^2-y^2}$) and a higher-energy triply degenerate t_2 set (d_{xy}, d_{yz}, d_{zx}). Since Mn^{5+} has a $3d^2$ configuration, the two electrons occupy the lower e states. As shown in Fig. 7, the occupied states near the Fermi level ($E \approx 0$ eV) are predominantly of e character, while the unoccupied states around 1.6 eV correspond to the t_2 orbitals. The fundamental origin of the coloration lies in the transition between these crystal-field-split levels. In an ideal centrosymmetric or perfectly tetrahedral environment, electric-dipole transitions between d states (d–d transitions) are parity-forbidden by the Laporte selection rule. If the local symmetry were perfectly T_d, the transition probability would be negligible, as confirmed by the unoptimized spectrum in Fig. 6. However, as evidenced by our structural optimization, the $[MnO_4]^{3-}$ tetrahedron undergoes significant distortion (C_1 symmetry). This symmetry breaking is the decisive factor. It allows for the mixing of the odd-parity O 2p ligand orbitals into the even-parity Mn 3d states (p–d hybridization). This hybridization relaxes the strict selection rules, imparting a finite and significant oscillator strength to the nominally forbidden $e \rightarrow t_2$ transition. It is this symmetry-lowering induced hybridization that generates the intrinsic absorption moment. Consequently, even when the macroscopic optical properties are averaged over random orientations as in a powder sample, the absorption peak at 1.6 eV remains robust and distinct. The distortion "activates" the optical transition across the visible range, resulting in the vivid blue reflection observed in the Mn-doped $Ba_3V_2O_8$ pigment.

4. Conclusion

In conclusion, this study has provided a comprehensive theoretical framework to understand the electronic and optical properties of Mn-doped $Ba_3V_2O_8$. Our first-principles calculations demonstrated that the substitution of vanadium with manganese introduces Mn 3d impurity states within the band gap of the host material. These mid-gap states arise intrinsically from the $3d^2$ electronic configuration of the Mn^{5+} ion, where the occupied e states and unoccupied t_2 states are separated by the crystal field splitting. Furthermore, the structural relaxation revealed that the $[MnO_4]^{3-}$ tetrahedron undergoes significant distortion compared to the ideal geometry. This structural distortion plays a critical role not in creating the impurity levels, but in governing the optical transition probabilities. The lowering of local symmetry enhances the hybridization between Mn 3d and O 2p orbitals, thereby relaxing the optical selection rules. This symmetry-breaking mechanism "activates" the nominally forbidden d–d transition, imparting it with finite oscillator strength. Consequently, a characteristic absorption peak at 1.6 eV emerges and remains robust even in the orientation-averaged spectrum representing the powder form of the pigment. Ultimately, this work elucidates that while the Mn^{5+} electronic configuration dictates the potential for color centers, the local lattice distortion is the key trigger that intensifies the optical absorption, giving rise to the vivid blue coloration of Mn-doped $Ba_3V_2O_8$.

References

1) European Parliament and Council, Directive 2002/95/EC of the European Parliament and of the Council of 27 January 2003 on the restriction of the use of certain hazardous substances in electrical and electronic equipment. Official Journal of the European Union, L37, 19–23 (2003).
2) A. E. Smith, M. C. Comstock and M. A. Subramanian, *Dyes Pigments* 133, 214 (2016).
3) E. A. Medina, J. Li, J. K. Sralick and M. A. Subramanian, *Solid State Sci.* 52, 97 (2016).
4) S. Laha, S. Tamilarasan, S. Natarajan and J.

Gopalakrishnan, *Inorg. Chem.* 55, 3508 (2016).
5) S. W. Kim, G. E. Sim, J. Y. Pck, J. H. Son, T. Hasegawa, K. Toda and D. S. Bae, *Dyes Pigments* 139, 344 (2017).
6) Y. Wang, H. Lei, P. Jiang, L. Liu, K. Cui and W. Cao, *Ceram. Int.* 47, 686 (2021).
7) H. Guo, L. Yuan, S. Wang and C. Hou, *Ceram. Int.* 50, 3110 (2024).
8) H. Kojima, J. Ishii and S. Matsushima, *Research Report of Kitakyushu National College of Technology* 58, 21 (2024) [in Japanese].
9) S. Fop, J. A. Dawson, D. N. Tawse, M. G. Skellern, J. M. S. Skakle and A. C. Mclaughlin, *Chem. Mater.* 34, 8190 (2022).
10) V. Milman, B. Winkler, J. A. White, C. J. Pickard, M. C. Payne, E. V. Akhmatskaya and R. H. Nobes, *Int. J. Quantum Chem.* 77, 895910 (2000).
11) J. P. Perdew and Y. Wang, *Phys. Rev. B* 45, 13244 (1992).
12) J. P. Perdew, K. Burke and M. Ernzerhof, *Phys. Rev. Lett.* 77, 38653868 (1996).
13) D. Vanderbilt, *Phys. Rev. B* 41, 7892 (1990).
14) H. J. Monkhorst and J. D. Pack, *Phys. Rev. B* 13, 5188 (1976).
15) P. Blaha, K. Schwarz, G. K. H. Madsen, D. Kvasnicka and J. Luitz, in "WIEN2k, An Augmented Plane Wave + Local Orbitals Program for Calculating Crystal Properties", Ed. by K. Schwarz, Techn. Universitat Wien, Austria (2001) ISBN 3-9501031-1-2.
16) P. Blaha, K. Schwarz, F. Tran, R. Laskowski, G. K. H. Madsen and L. D. Marks, *J. Chem. Phys.* 152, 74101 (2020).
17) C. Ambrosch-Draxl and J. Sofo, *Comput. Phys. Commun.* 175, 1 (2006).
18) Y. Obukuro, K. Ninomiya, M. Arai, Y. Okuyama, G. Sakai and S. Matsushima, *Comp. Mater. Sci.* 126, 7 (2017).
19) G. I. Csonka, J. P. Perdew, A. Ruzsinszky, P. H. T. Philipsen, S. Lebègue, J. Paier, O. A. Vydrov and J. G. Ángyán, *Phys. Rev. B* 79, 155107 (2009).
20) W. Setyawan and S. Curtarolo, *Comp. Mater. Sci.* 49, 299 (2010).
21) R. O. Jones and O. Gunnarsson, *Rev. Mod. Phys.* 61, 689 (1989).
22) P. Mori-Sánchez, A. J. Cohen and W. T. Yang, *Phys. Rev. Lett.* 100, 146401 (2008).
23) J. Wiktor, I. Reshetnyak, F. Ambrosio and A. Pasquarello, *Phys. Rev. Mater.* 1, 022401(R) (2017).
24) T. D. H. Nguyen, V. K. Dien, H. D. Pham, T. M. D. Huynh and M.-F. Lin, *Comp. Mater. Sci.* 198, 110675 (2021).